

Room-Temperature Polar Ferromagnet ScFeO_3 Transformed from a High-Pressure Orthorhombic Perovskite Phase

Takahiro Kawamoto,[†] Koji Fujita,^{*,†} Ikuya Yamada,^{‡,§} Tomohiko Matoba,[†] Sung Joo Kim,^{||} Peng Gao,^{||} Xiaoqing Pan,^{||} Scott D. Findlay,[⊥] Cédric Tassel,^{#,∇} Hiroshi Kageyama,[#] Andrew J. Studer,[○] James Hester,[○] Tetsuo Irifune,[◆] Hirofumi Akamatsu,[¶] and Katsuhisa Tanaka[†]

[†]Department of Material Chemistry, Graduate School of Engineering, Kyoto University, Katsura, Nishikyo-ku, Kyoto 615-8510, Japan

[‡]Nanoscience and Nanotechnology Research Center, Osaka Prefecture University, 1-2 Gakuen-cho, Sakai, Osaka 599-8531, Japan

[§]PRESTO, Japan Science and Technology Agency (JST), Chiyoda-ku, Tokyo 102-0075, Japan

^{||}Department of Materials Science and Engineering, University of Michigan, Ann Arbor, Michigan 48109, United States

[⊥]School of Physics, Monash University, Melbourne, Victoria 3800, Australia

[#]Department of Energy and Hydrocarbon Chemistry, Graduate School of Engineering, Kyoto University, Katsura, Nishikyo-ku, Kyoto 615-8510, Japan

[∇]The Hakubi Center for Advanced Research, Kyoto University, Yoshida-Ushinomiya-cho, Sakyo-ku, Kyoto 606-8302, Japan

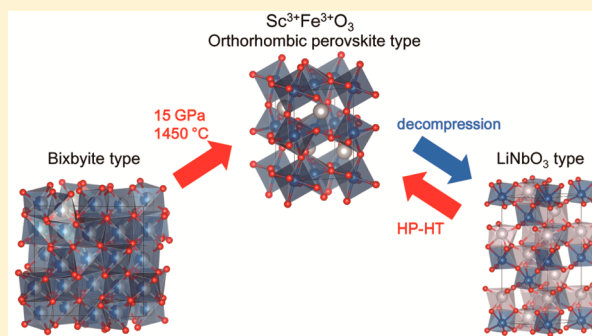
[○]Bragg Institute, Australian Nuclear Science and Technology Organisation, PMB 1, Menai, New South Wales 2234, Australia

[◆]Geodynamics Research Center, Ehime University, 2-5, Bunkyo-Cho, Matsuyama 790-8577, Japan

[¶]Materials Research Institute and Department of Materials Science and Engineering, Pennsylvania State University, University Park, Pennsylvania 16802, United States

Supporting Information

ABSTRACT: Multiferroic materials have been the subject of intense study, but it remains a great challenge to synthesize those presenting both magnetic and ferroelectric polarizations at room temperature. In this work, we have successfully obtained LiNbO_3 -type ScFeO_3 , a metastable phase converted from the orthorhombic perovskite formed under 15 GPa at elevated temperatures. A combined structure analysis by synchrotron X-ray and neutron powder diffraction and high-angle annular dark-field scanning transmission electron microscopy imaging reveals that this compound adopts the polar $R3c$ symmetry with a fully ordered arrangement of trivalent Sc and Fe ions, forming highly distorted ScO_6 and FeO_6 octahedra. The calculated spontaneous polarization along the hexagonal c -axis is as large as $100 \mu\text{C}/\text{cm}^2$. The magnetic studies show that LiNbO_3 -type ScFeO_3 is a weak ferromagnet with $T_N = 545 \text{ K}$ due to a canted G -type antiferromagnetic ordering of Fe^{3+} spins, representing the first example of LiNbO_3 -type oxides with magnetic ordering far above room temperature. A comparison of the present compound and rare-earth orthorhombic perovskites RFeO_3 ($\text{R} = \text{La-Lu}$ and Y), all of which possess the corner-shared FeO_6 octahedral network, allows us to find a correlation between T_N and the Fe-O-Fe bond angle, indicating that the A-site cation-size-dependent octahedral tilting dominates the magnetic transition through the Fe-O-Fe superexchange interaction. This work provides a general and versatile strategy to create materials in which ferroelectricity and ferromagnetism coexist at high temperatures.



1. INTRODUCTION

Perovskite-type ABO_3 transition metal oxides (B = transition metal) with a framework of corner-shared BO_6 octahedra enclosing the A-site cations have provided a rich variety of useful functions such as ferroelectricity, superconductivity, and ferromagnetism and also have been considered as a major candidate for multiferroic materials that simultaneously exhibit magnetic and ferroelectric ordering. Such a richness of physical properties in the perovskite oxides arises from their capacity to adopt a multitude of different structural distortions due to the

possible incorporation of A- and B-site cations of a wide range of ionic radii and valence states.^{1,2}

Nevertheless, polar and magnetic perovskite oxides are very scarce because of the contradicting requisites: ferroelectric B-site cation off-centering requires empty d orbitals (d^0 electronic configurations), while the ferromagnetism requires B-site cations with partially filled d orbitals (non- d^0 electronic

Received: August 4, 2014

Published: October 21, 2014

configurations) which favor in general a symmetric coordination environment.³ One approach to tackle this problem is to select materials containing lone-pair active cations, like Bi^{3+} or Pb^{2+} , at the A-site, where the stereochemical effect of $6s^2$ lone pair electrons induces a polar structure. However, only a limited number of magnetic ferroelectrics of this kind are known, such as BiFeO_3 , BiMnO_3 , $\text{Bi}_2\text{NiMnO}_6$, BiCoO_3 , and PbVO_3 .^{4–9} An alternative approach is to select materials with unusually small A-site cations.^{10–31} Examples include the polar LiNbO_3 -type compounds with $R3c$ symmetry, MnTiO_3 and FeTiO_3 , which can be viewed as grossly distorted perovskite structures with small tolerance factors (t). The polar structure is characterized by out-of-phase tilting of corner-shared BO_6 octahedra around the 3-fold pseudocubic $[111]$ axis (Glazer notation $a^-a^-a^-$ ^{32,33}) with cation displacements along the $[111]$ direction driven by the coordination preference of the small A-site cations,^{34,35} which induces a spontaneous polarization in the $[111]$ direction. Note that the LiNbO_3 -type structure is also viewed as an ordered derivative of corundum-type structure.¹ This approach does not necessarily involve d^0 transition metals or lone-pair active cations (e.g., MnSnO_3 ,^{11,15,25} ZnSnO_3 ,²¹ and PbNiO_3 ²⁴) and thus enables more flexible design of polar magnetic materials, although high-pressure and high-temperature conditions are often needed to stabilize the framework of strongly tilted BO_6 octahedra so as to accommodate the small A-site cations.

So far, perovskite oxides with small A-site cations have been exploited to create polar magnetic materials, but all of them exhibit magnetic ordering below room temperature (rt).^{10,11,22–26,28,29,31} Here, we have examined the phase evolution of ScFeO_3 under high-pressure and high-temperature conditions and successfully synthesized a new polar material that exhibits weak ferromagnetic ordering far above rt ($T_N = 545$ K). It is known that, under ambient conditions, ScFeO_3 adopts a nonperovskite phase (bixbyite-type structure) due to the “too small” ionic size of Sc^{3+} . Li et al.³⁶ recently reported that the bixbyite-type ScFeO_3 transforms into the corundum-type structure at 6 GPa and 1500 °C. They also showed the presence of the polar nature in the corundum phase, although the corundum structure itself (space group $R\bar{3}c$) must be centrosymmetric and nonpolar due to the random distribution of cations. In the “polar” corundum-type ScFeO_3 , the degree of cation ordering is very small and the magnetic transition temperature is much lower ($T_N = 365$ K). We have found through in situ X-ray diffraction (XRD) that the application of higher pressure (~ 15 GPa) at temperatures above 800 °C leads to the formation of an orthorhombic perovskite. The orthorhombic perovskite is unquenchable to ambient conditions but recovered to the LiNbO_3 -type structure while preserving the BO_6 network. The fully ordered arrangement of Sc^{3+} and Fe^{3+} ions in the LiNbO_3 -type structure is conclusively confirmed by direct observation in high-angle annular dark-field scanning transmission electron microscopy (HAADF-STEM) images. This new compound is the first example of LiNbO_3 -type oxide where the magnetic ordering occurs above rt. Comparative studies between LiNbO_3 -type ScFeO_3 and orthorhombic perovskite-type RFeO_3 ($\text{R} = \text{La–Lu}$ and Y) have revealed an intimate link between the structural and magnetic properties in the whole series.

2. EXPERIMENTAL PROCEDURES

Bixbyite-type ScFeO_3 , a stable phase of this composition under ambient conditions, was prepared from a stoichiometric mixture of

Sc_2O_3 (99.9%, previously heated to 1000 °C) and Fe_2O_3 (99.99%) powders using the conventional solid-state reaction at 1400 °C for 24 h under ambient pressure, which was used as the precursor for high-pressure synthesis. After the single-phase sintered ScFeO_3 was ground, the resultant powder was charged into a Pt capsule and put into a high-pressure cell. The high-pressure and high-temperature treatment was carried out at 15 GPa and 1450 °C using a Kawai-type high-pressure apparatus. After being treated for 30 min, the temperature was quickly cooled to rt followed by the slow release of the pressure.

The product was initially identified at room temperature by the XRD analysis using a Rigaku RINT2500 diffractometer with $\text{Cu } K_\alpha$ radiation ($\lambda = 1.5406$ Å). For the structural refinement, synchrotron XRD (SXR) data were collected at rt using a large Debye–Scherrer camera with an imaging-plate-type detector, installed in the BL02B2 beamline at SPring-8. The incident beam was monochromated at $\lambda = 0.41913$ Å. The finely ground powder sample was housed in a Lindemann glass capillary tube with an inner diameter of 0.2 mm and was continuously rotated during measurements to reduce the effect of preferential orientation. The structural parameters were refined by the Rietveld analysis using the program RIETAN-FP.³⁷ The neutron powder diffraction (NPD) data were recorded using the high-intensity powder diffractometer WOMBAT at ANSTO’s OPAL facility. The incident neutron wavelength was $\lambda = 2.7168$ Å. The sample (20 mg) was sealed in a He-filled vanadium can. The crystal and magnetic structures were refined by the Rietveld analysis using JANA2006.³⁸ The sample was also characterized by HAADF-STEM imaging and optical second-harmonic generation (SHG). The HAADF images were taken with an aberration-corrected STEM (JEOL 2100F with probe correction) and interpreted through comparison with simulations based on the frozen phonon method.³⁹ The SHG response was tested at rt using a pulsed Nd:YAG laser (λ , 1064 nm; pulse duration, 25 ps; repetition rate, 10 Hz) as the light source. The crystal and magnetic structures were drawn using the program VESTA.⁴⁰

To probe the structural transformation of ScFeO_3 under high pressure, in situ SXR experiments were performed using a Kawai-type apparatus SPEED-1500 installed in the BL04B1 beamline at SPring-8.⁴¹ White X-ray was used as the incident beam and a solid-state germanium detector was utilized for data collection. The X-rays diffracted from the sample were collected at a fixed 2θ angle of about 5° by the energy dispersive method. The MgO sleeve, in which the sample was enclosed, was used as the pressure marker. The applied pressure was calculated from the lattice parameters of MgO using an equation of state.⁴²

The magnetic susceptibility was recorded on a SQUID magnetometer (Quantum Design, MPMS) between 300 and 600 K under zero-field-cooling (ZFC) and field-cooling (FC) conditions at an external magnetic field of 1 kOe. The magnetic-field dependence of magnetization was measured at 5, 300, 540, and 550 K by changing the magnetic field between -10 and 10 kOe. ^{57}Fe Mössbauer spectroscopy was performed at rt and 553 K in the transmission geometry by employing ^{57}Co in metallic Rh as a γ -ray source. The velocity scale was calibrated by using a spectrum of α -Fe foil measured at rt. The isomer shift was given with respect to α -Fe. The obtained spectra were fitted by a least-squares method using the Lorentzian function.

3. RESULTS

3.1. Crystal Structure. The laboratory XRD pattern on the sample recovered from 15 GPa and 1450 °C revealed the formation of ScFeO_3 in the rhombohedral symmetry. Unless otherwise addressed, we will hereafter use the hexagonal setting. Figure 1 shows the SXR pattern at rt and the result of the Rietveld analysis. The reflection conditions observed are $-h + k + l = 3n$ for $hkil$, $h + l = 3n$ and $l = 2n$ for $h\bar{h}0l$, $l = 3n$ for $hh\bar{2}hl$, and $l = 6n$ for $000l$ (obverse setting), which are compatible with either noncentrosymmetric polar $R3c$ (No. 161) or centrosymmetric nonpolar $R\bar{3}c$ (No. 167) space groups. There were several unknown peaks with intensities less

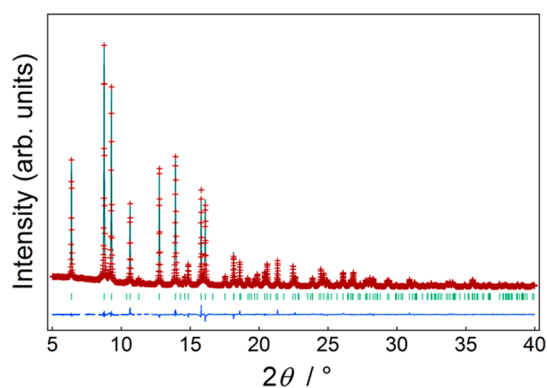


Figure 1. Rietveld refinement of room-temperature SXRDX data ($\lambda = 0.41913 \text{ \AA}$) for ScFeO_3 recovered from 15 GPa and 1450 °C based on the LiNbO_3 -type structure, showing the observed (crosses) and calculated (solid line) profiles. The bottom solid line represents the difference between the observed and calculated profiles. The ticks correspond to the positions of the calculated Bragg reflections for LiNbO_3 -type ScFeO_3 .

than 4% of the main peak of the rhombohedral phase (see the Supporting Information, Figure S1). The unknown peaks were excluded in the structure refinement. The Rietveld refinement was carried out on the basis of a completely cation-ordered LiNbO_3 -type structure (noncentrosymmetric polar) and a cation-disordered corundum-type structure (centrosymmetric nonpolar). Both refinements converged well with a weighted reliability factor of $R_{\text{wp}} = 4.166\%$ for the former and $R_{\text{wp}} = 4.567\%$ for the latter. It is almost impossible to determine unambiguously the crystal symmetry from the SXRDX analysis alone because of the similar X-ray scattering factors of Sc and Fe.

In order to find a clue for the order/disorder of Sc and Fe, we measured an optical SHG at rt using 1064 nm radiation. An SHG response was clearly observed on the ungraded powder sample (average particle size of 19 μm ; see Supporting Information, Figure S2), indicating that the present compound is acentric because the SHG properties are related to a third-rank polar tensor. The SHG efficiency is approximately 2 times larger than that of $\alpha\text{-SiO}_2$ powder in the same particle size

range (20–45 μm). Note that the SHG efficiency for ScFeO_3 is underestimated by both the absorption of 1064 nm incident light and the reabsorption of 532 nm emitted (SHG) light, as revealed by the diffuse reflectance measurement (see Supporting Information, Figure S3). We further conducted HAADF-STEM to directly observe the arrangement of Sc and Fe ions. Parts a and b of Figure 2 display, respectively, the HAADF image and the LiNbO_3 -type structure in the $[uvw] = [\bar{1}101]$ projection. Comparison of the projected structure with the HAADF image, in which the intensity is expected to scale approximately as the square of the atomic number Z , reveals that only the Sc and Fe columns are visible. The O columns ($Z = 8$) are not visible because their small atomic number means that they scatter much more weakly than the heavier Sc ($Z = 21$) and Fe ($Z = 26$) columns. It is noticed from the projected LiNbO_3 -type structure that the Sc and Fe ions form alternate layers along the $[0001]$ direction, producing dumbbells in which one column in the pair is pure Sc and the other pure Fe. Conversely, the corundum-type structure would have the same basic atom sites but would have a random (and thus approximately equal) distribution of Sc and Fe atoms in both columns in each dumbbell. Although characterization of the experimental setup did not allow unambiguous separation of the effects of thickness, probe-size, and concentration, the clear and consistent difference between the intensities of the two columns in the dumbbells in the HAADF image (Figure 2a,c) provides direct evidence favoring the LiNbO_3 -type structure over the corundum-type structure. This interpretation is further supported by the HAADF image simulations, which show that the intensities of the two columns in the dumbbell are indistinguishable in the corundum-type structure [Figure 2a (inset),d], whereas the perfectly ordered LiNbO_3 -type structure [Figure 2a (inset),e] gives intensities in good agreement with the experimental data, with the high and low brightness peaks corresponding to Fe and Sc columns, respectively. The HAADF result in the present study is in marked contrast to the case of the “polar” corundum ScFeO_3 prepared at the lower pressure of 6 GPa, where the HAADF image showed the disordered Sc/Fe arrangement; in the polar corundum, a small degree of cation ordering was detected by convergent-beam electron diffraction (CBED).³⁶

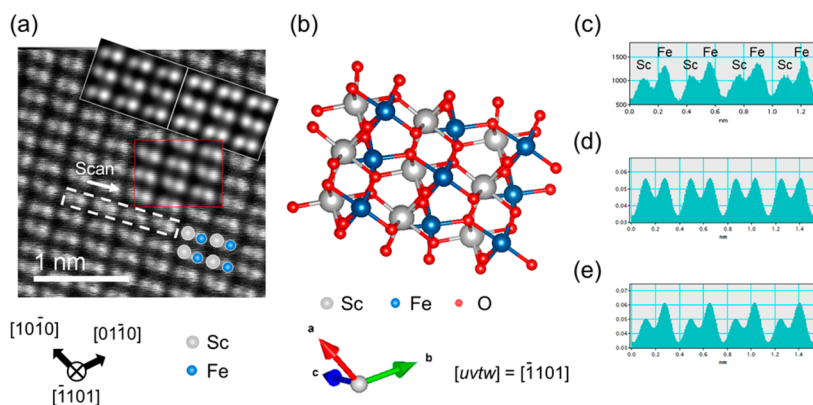


Figure 2. (a) HAADF-STEM image in the $[\bar{1}101]$ projection for ScFeO_3 recovered from 15 GPa and 1450 °C. White and dark spheres represent Fe and Sc ions, respectively. Simulated images for the ordered LiNbO_3 -type (white border, left) and random corundum-type structure (white border, right) are inset as is a copy of the experimental image averaged over the repeating unit (red border). (b) Schematic illustration of the crystal structure of LiNbO_3 -type ScFeO_3 in the $[\bar{1}101]$ projection. The white, blue, and red spheres indicate Sc, Fe, and O ions, respectively. (c) Line scan intensity profiles projected over the dashed white rectangle in part a and simulated intensity profiles based on (d) random corundum-type structure and (e) LiNbO_3 -type structure.

On the basis of the LiNbO₃-type structure, we performed Rietveld refinement of NPD data at 300 and 5 K, the result of which will be demonstrated separately in section 3.4. For both profiles, the magnetic diffraction peaks were observed at low angles, and therefore, the magnetic structure was considered in the refinement. When the occupancy factors, *g*, of Sc, Fe, and O were allowed to vary, they remained approximately unity [*g*(Sc) = 0.98(6), *g*(Fe) = 0.94(6), and *g*(O) = 1.10(7)], confirming the fully Sc/Fe ordering as well as the absence of oxygen deficiency. Complementary elemental analysis using inductively coupled plasma (ICP) showed a cationic ratio of Sc_{0.986}Fe_{1.014}, consistent with the nominal composition within the expected errors. Hence, the site occupancies were fixed at unity for all the sites in the final refinements on both SXR and NPD.

A polyhedral representation of the crystal structure refined with SXR data is shown in Figure 3a, and the final structural

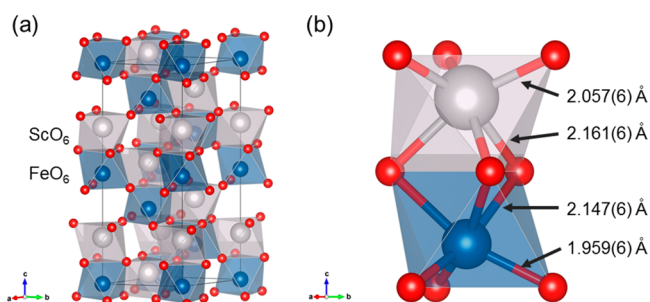


Figure 3. (a) Polyhedral representation of the crystal structure for LiNbO₃-type ScFeO₃. White and blue spheres represent Sc and Fe atoms, respectively. (b) Local coordination environment of ScO₆ and FeO₆ octahedra stacked along the *c*-axis, showing a face-sharing octahedral pair.

parameters are tabulated in Table 1. The calculated density is significantly larger for the LiNbO₃-type ScFeO₃ (4.548 g/cm³) than for the bixbyite-type ScFeO₃ (4.401 g/cm³),⁴³ consistent with the expectation that a high-pressure synthesis provides a higher-density phase. Notably, LiNbO₃-type ScFeO₃ has a denser structure than the “polar” corundum-type phase (4.513

Table 1. Refined Lattice and Structural Parameters for LiNbO₃-Type ScFeO₃ Obtained from SXR (rt) and NPD (5 and 300 K) Data^a

atom	rt (SXR)	300 K (NPD)	5 K (NPD)
<i>a</i> /Å	5.1968(2)	5.1994(9)	5.1971(4)
<i>c</i> /Å	13.9363(5)	13.947(2)	13.9203(17)
Sc			
<i>z</i>	0.21050(6)	0.2168(7)	0.21213(12)
<i>B</i> _{iso} /Å ²	0.26(4)	0.9(1.2)	0.6(5)
Fe			
<i>B</i> _{iso} /Å ²	0.42(3)	0.2(1.4)	0.8(7)
<i>μ</i> / <i>μ</i> _B		3.53(14)	3.71(10)
O			
<i>x</i>	0.0161(11)	−0.01(2)	0.019(6)
<i>y</i>	0.3112(8)	0.290(7)	0.307(4)
<i>z</i>	0.1045(5)	0.1067(7)	0.10271(12)
<i>B</i> _{iso} /Å ²	0.56(4)	0.2(5)	0.01(0.24)
<i>R</i> _{wp} /%	4.166	2.05	1.45
<i>R</i> _p /%	3.089	1.52	1.10
<i>R</i> _B /%	1.306	5.14	5.96
goodness of fit	0.7877	2.96	3.38

^aHexagonal, space group *R*3*c* (No. 161), *Z* = 6, with atoms in the following positions: Sc, 6*a* (0, 0, *z*); Fe, 6*a* (0, 0, 0); O, 18*b* (*x*, *y*, *z*). The occupancy parameter *g* is fixed to unity for all the atoms.

g/cm³) stabilized at 6 GPa,³⁶ implying a remarkable difference in the cation arrangement between the two compounds. The bond valence sum (BVS)⁴⁴ calculated from the structural parameters is 3.00 and 2.80 for Sc and Fe, respectively, in accordance with the formal ionic composition of Sc³⁺Fe³⁺O₃. The coordination environment for the adjacent Sc and Fe sites along the hexagonal *c*-axis is displayed in Figure 3b, and the selected bond lengths and angles are listed in Table 2. The

Table 2. Selected Bond Lengths and Bond Angle Obtained from the Refinement of Room-Temperature SXR Data

Sc–O (×3)/Å	2.057(6)
Sc–O (×3)/Å	2.161(6)
Fe–O (×3)/Å	2.147(6)
Fe–O (×3)/Å	1.959(6)
Fe–O–Fe/deg	135.1(3)
<i>φ</i> ^a /deg	30
<i>Δ</i> ^b of ScO ₆	6.1 × 10 ^{−4}
<i>Δ</i> ^b of FeO ₆	21.0 × 10 ^{−4}

^aTilting angle of FeO₆ octahedra about the hexagonal *c*-axis (i.e., 3-fold pseudocubic [111] axis) calculated from the lattice parameter.¹
^bOctahedral distortion parameter $\Delta = 1/6 \sum [(d_i - \langle d \rangle) / \langle d \rangle]^2$, where *d*_{*i*} is the individual bond distance and *d* is the average bond length.

tilting angle of FeO₆ octahedra about the hexagonal *c*-axis (or equivalently, 3-fold pseudocubic [111] axis), *φ*, and the octahedral distortion parameter, *Δ*, were also calculated, as shown in Table 2. These parameters are discussed in section 4.2.

3.2. Phase Evolution under High Pressure and High Temperature. It has been reported that some LiNbO₃-type oxides are stabilized via the orthorhombically distorted perovskites under high-pressure and high-temperature conditions.^{14,15,19} To examine the phase evolution of ScFeO₃, we performed in situ XRD measurements. Figure 4a shows the in situ XRD patterns of ScFeO₃ at rt and 800 °C under a pressure of 14.8 GPa. The bixbyite-type phase was initially compressed to 14.8 GPa at rt, and then the temperature was increased to 800 °C under a constant press load. At rt and 14.8 GPa, the bixbyite-type structure is retained, although diffraction peaks become broader. Upon heating, we observed the appearance of diffraction patterns that can be indexed in an orthorhombic perovskite unit cell with the space group of *Pnma* (No. 62) or *Pn2₁a* (No. 33). As shown in Figure 4b, the LiNbO₃-type ScFeO₃ reverts back to the orthorhombic perovskite upon compression to 14.8 GPa at rt. Thus, the LiNbO₃-type ScFeO₃ is quenched as a metastable phase through the transformation from the high-pressure orthorhombic perovskite structure. It should be mentioned that the orthorhombic or monoclinic perovskites ScBO₃ (B = V,⁴⁵ Cr,^{46,47} Mn,⁴⁸ and Rh⁴⁹) have been synthesized as quenchable phases via high-pressure and high-temperature treatments. The phase transformation of orthorhombic perovskite to LiNbO₃-type structure in ScFeO₃ may be related to the half-filled 3d⁵ electron configuration of Fe³⁺, but further investigation is required to clarify this phenomenon.

3.3. Magnetic Properties. Figure 5a shows the temperature dependence of magnetic susceptibility *χ*(*T*) of LiNbO₃-type ScFeO₃, measured at *H* = 1 kOe in ZFC and FC modes. As *T* is decreased, *χ* rises abruptly around 545 K, and a branch between ZFC and FC is observed at 540 K. For *T* > 545 K, LiNbO₃-type ScFeO₃ is paramagnetic, as revealed by a linear

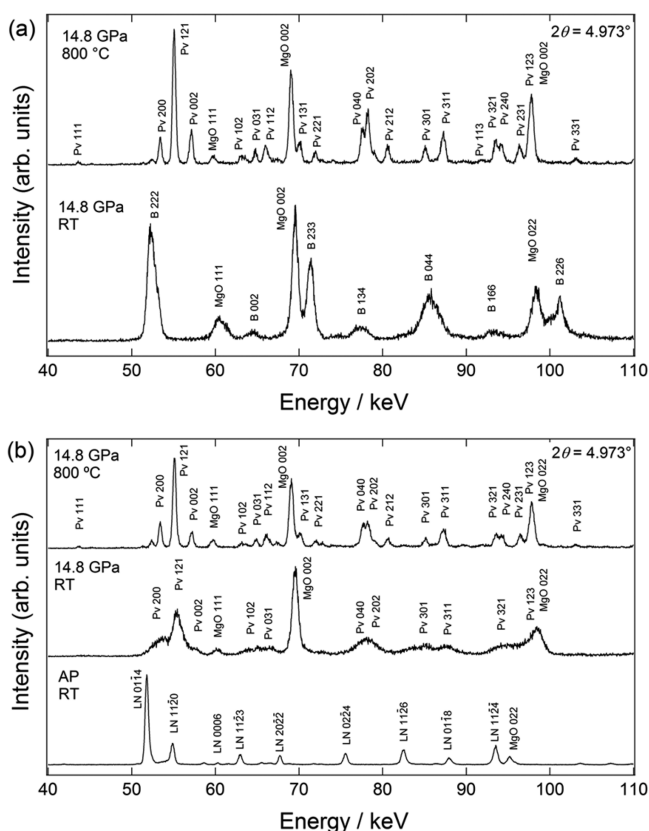


Figure 4. In situ XRD patterns of ScFeO_3 measured by the energy-dispersive method: (a) a pressure of 14.8 GPa was applied to the bixbyite-type ScFeO_3 at rt and the temperature was increased to 800 °C; (b) a pressure of 14.8 GPa was applied to the as-prepared LiNbO_3 -type ScFeO_3 at rt and the temperature was increased to 800 °C. Abbreviations are as follows: B, bixbyite; Pv, perovskite; LN, lithium niobate; MgO, pressure maker; AP, ambient pressure.

isothermal magnetization curve (M – H curve) at 550 K (see Figure 5b). For $T < 545$ K (540, 300, and 5 K), a clear hysteresis loop appears in the M – H curve, although the linear increase in M is observed up to $H = 10$ kOe. A tiny jump of M in the low-field region ($H \sim 100$ Oe) may be ascribed to a spin-flop transition. The saturated moment at 5 K is estimated to be about $0.035\mu_{\text{B}}/\text{Fe}$, which is significantly lower than the spin moment of high-spin Fe^{3+} ($5\mu_{\text{B}}$). Thus, the abrupt rise of χ below 545 K as shown in Figure 5a is accounted for by a weak ferromagnetism (or canted antiferromagnetism). The Néel temperature estimated from the inflection point in the χ – T plot is $T_{\text{N}} = 545$ K, which is surprisingly higher than that of the “polar” corundum ScFeO_3 ($T_{\text{N}} = 356$ K).³⁰ Given the absence of the inversion center on Fe–O–Fe bonds in LiNbO_3 -type ScFeO_3 , the weakly ferromagnetic component could be caused by the canting of the antiferromagnetically coupled Fe^{3+} moments via the antisymmetric exchange driven by the Dzyaloshinskii-Moriya (DM) interaction.^{50,51}

3.4. Magnetic Structure. The magnetic ordering at rt is verified by the Mössbauer spectrum with a well-split sextet (Figure 6a). A minor doublet (4 area %) possibly arises from an unidentified magnetic impurity. Upon heating to 553 K, the sextet changes to a paramagnetic doublet (Figure 6b). The Mössbauer parameters obtained by the least-squares fitting are summarized in Table 3. A high-spin state of Fe^{3+} manifests itself in the hyperfine field (HF = 47.3 T) and isomer shift (IS = 0.41 mm s^{-1}) at rt. The $S_1 - S_2$ value of 0.40 mm s^{-1} as observed in

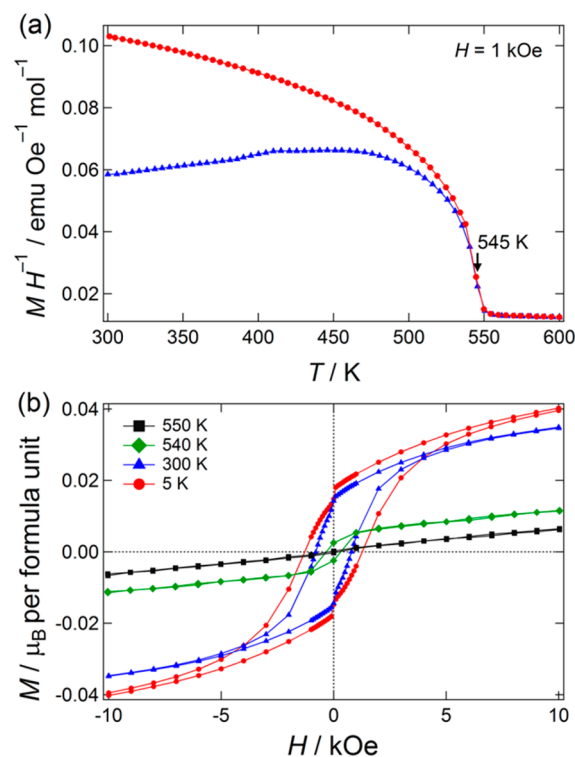


Figure 5. (a) Temperature dependence of magnetic susceptibility, $\chi = M/H$, of LiNbO_3 -type ScFeO_3 measured at $H = 1$ kOe under ZFC and FC conditions. (b) M – H curves at various temperatures between 5 and 550 K.

the Mössbauer spectrum at rt is close to the quadrupole splitting ($QS = 0.46 \text{ mm s}^{-1}$) at 553 K, indicating that the ordered Fe^{3+} moments align perpendicularly to the hexagonal c -axis, corresponding to the principal axis of the electric field gradient.⁵² Remarkably, this QS value is an order of magnitude larger than those for the orthorhombic perovskites RFeO_3 ($R = \text{La-Lu}$ and Y) with nearly regular FeO_6 octahedra.⁵³ This means that the octahedral Fe^{3+} ions in the present compound are highly off-centered, as validated by the final structure refined.

The NPD pattern at 5 K is displayed in Figure 7a. The observed peaks can be indexed by using the crystal structure as described above, but forbidden peaks are additionally observed at the low angles, such as those at $2\theta = 34^\circ$ (0003 reflection) and 37° ($10\bar{1}1$ reflection). The magnetic origin of these additional peaks is supported by the decreased peak intensity upon heating to 300 K (Figure 7b). We utilized the representation analysis performed for LiNbO_3 -type MnTiO_3 , leading to two G -type antiferromagnetic models, where the nearest-neighbors spins are antiparallel and aligned within the ab -plane or along the c -axis.⁵⁴ Figure 7c compares the refinement results with different spin directions and using the crystallographic data based on the LiNbO_3 -type structure. The better fit was obtained when the spins are aligned within the ab -plane as depicted in Figure 8. This result agrees with that derived from the analysis of Mössbauer spectra, as mentioned above. Note that the spin direction in the ab -plane is not determined in this analysis. The refined magnetic moment is found to be $\mu = 3.53(14)\mu_{\text{B}}/\text{Fe}$ at 300 K and $\mu = 3.71(10)\mu_{\text{B}}/\text{Fe}$ at 5 K. The weak ferromagnetic component evaluated from the M – H curve at 5 K (see Figure 5b) is $0.035\mu_{\text{B}}/\text{Fe}$, corresponding to the canting angle of 0.2° . Determination of

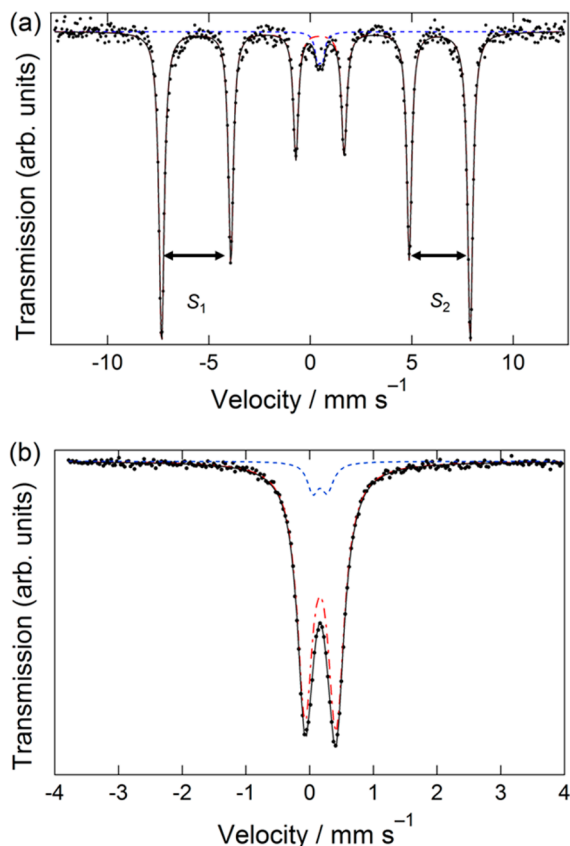


Figure 6. Mössbauer spectra of LiNbO₃-type ScFeO₃ at (a) room temperature and (b) 553 K. The dots represent the experimental data and the solid lines the total fits including the contributions from LiNbO₃-type ScFeO₃ (red dashed and dotted line) and paramagnetic impurity (blue broken lines). In part a, S₁ and S₂ denote the relative shifts of the peaks.

Table 3. Hyperfine Parameters of Mössbauer Spectra for LiNbO₃-Type ScFeO₃^a

temp	IS/mm s ⁻¹	QS/mm s ⁻¹	HF/T	A/%
rt	0.41	0.40 ^b	47	96
553 K	0.17	0.46	0	96 ^c

^aIS, QS, and HF denotes the isomer shift, quadrupole splitting, and hyperfine field, respectively, and A represents the area percent of the total fit. ^bQS at rt is defined as a difference of S₁ and S₂, S₁ – S₂, as shown in Figure 6a. ^cDue to the difficulty in separating the single doublet into two components, i.e., contributions from LiNbO₃-type ScFeO₃ and paramagnetic impurity, we assumed in the fitting procedure that the area percent for the doublet of LiNbO₃-type ScFeO₃ at 553 K is the same as that for the room-temperature data.

such a small canting angle is beyond the capability of NPD refinement: a trial refinement involving the canting angle gave a ferromagnetic component of 0.7μ_B (equivalent to a 5.6° canting of 3.71μ_B moment) within the *ab*-plane, but without improving the *R* factors.

4. DISCUSSION

4.1. LiNbO₃-Type A³⁺B³⁺O₃. LiNbO₃-type ScFeO₃ is a rare example of LiNbO₃-type structure with trivalent A and B ions. In general, cation ordering in complex metal oxides can be achieved when there is a large difference in the charge and/or size of cations. Most of known LiNbO₃-type and ilmenite-type

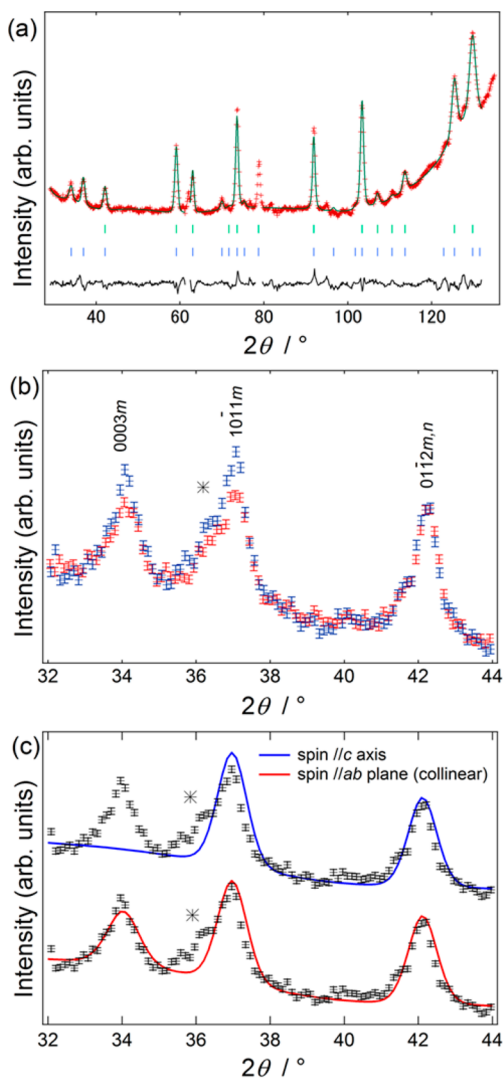


Figure 7. (a) Rietveld refinement of NPD data ($\lambda = 2.7168 \text{ \AA}$) for LiNbO₃-type ScFeO₃ at 5 K, showing the observed (crosses) and calculated (solid line) profiles. A vanadium peak at $2\theta \sim 79^\circ$ originating from the sample holder is excluded in the refinement. The bottom solid line represents the difference between the observed and calculated profiles. The two series of ticks correspond to the positions of the calculated nuclear (upper) and magnetic (lower) Bragg reflections. (b) Comparison of the NPD data in the low-angle region at 5 K (blue line) and 300 K (red line). The intensity is normalized to the 01 $\bar{1}$ 2 reflection. The peak marked by an asterisk is ascribed to the impurity phase that was also observed in our laboratory XRD. (c) Comparison of the Rietveld refinement of the magnetic structures in which spin lies along the *c*-axis (blue) and within the *ab*-plane with collinear arrangement (red).

compounds, which can be considered as ordered derivatives of corundum structure, follow this tendency, as exemplified by Li⁺Nb⁵⁺O₃ and Fe²⁺Ti⁴⁺O₃. Given the same oxidation state and similar ionic radii between Sc and Fe ions, it is not surprising to see that the corundum ScFeO₃ phase stabilized at 6 GPa and 1500 °C, as reported by Li et al.,³⁶ possesses a nearly random Sc/Fe arrangement. Once the orthorhombic perovskite is formed under high pressure, however, the cation ordering is expected to occur. This is what has been observed in scandium-based perovskites like ScVO₃,⁴⁵ ScCrO₃,^{46,47} ScMnO₃,⁴⁸ and ScRhO₃,⁴⁹ where the larger Sc³⁺ ions exhibit a strong preference for A-site occupation. Although the structural

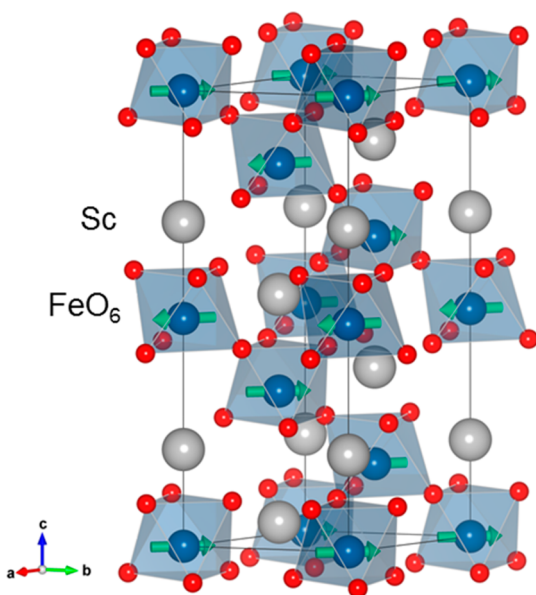


Figure 8. Magnetic structure of LiNbO₃-type ScFeO₃. The corner-shared FeO₆ octahedra are shown in blue and the Sc ions are represented by gray spheres. Arrows denote the direction of the magnetic moment of Fe³⁺.

refinement of in situ XRD profile was difficult because of poor data quality, we believe that the A-site preference of Sc³⁺ ions is realized in the high-pressure orthorhombic perovskite ScFeO₃ and that the cation distribution between the A-sites (Sc³⁺) and B-sites (Fe³⁺) is maintained during the transformation to the LiNbO₃-type structure upon decompression. Namely, a key to achieving the Sc³⁺/Fe³⁺ ordering in the LiNbO₃ structure is the stabilization of the orthorhombic perovskite under high pressure.

4.2. Structural Features. In ABO₃ perovskite oxides, the decrease in the A-site ionic radius results in the enhanced octahedral tilting, leading to the reduction in B–O–B bond angle. The Fe–O–Fe bond angle, α , of LiNbO₃-type ScFeO₃ and orthorhombic perovskite-type RFeO₃ (R = La–Lu and Y)^{55,56} is plotted in Figure 9 as a function of the A-site ionic radius (Shannon's six-coordinate ionic radius⁵⁷). The α value

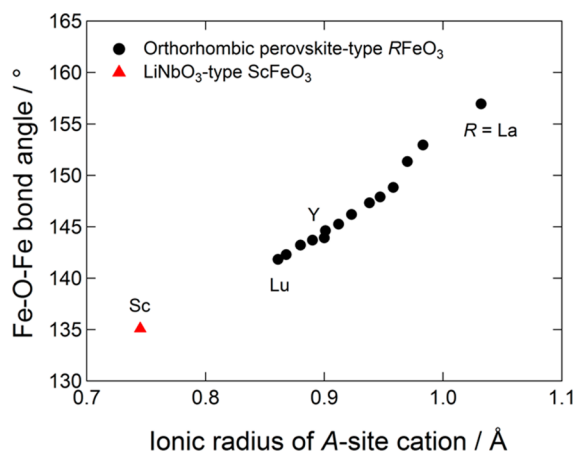


Figure 9. Dependence of the Fe–O–Fe bond angle on the ionic radius of A-site cations (in 6-fold coordination⁵⁷) for LiNbO₃-type ScFeO₃ (this work) and orthorhombic perovskite-type RFeO₃ (R = La–Lu and Y).^{55,56}

monotonically decreases with decreasing A-site ionic radius, and LiNbO₃-type ScFeO₃ takes the smallest value. What is distinct from orthorhombic perovskites RFeO₃ is the polar cation displacement in the LiNbO₃-type ScFeO₃: the Sc³⁺ ion moves into the octahedral site, and the ScO₆ octahedra shares a common face with the neighboring FeO₆ octahedra (see Figure 3b). The cation–cation repulsion across the shared face pushes the Fe³⁺ ion away from the face in the direction parallel to the *c*-axis. As seen from Table 2, the octahedral distortion is $\Delta = 21.0 \times 10^{-4}$ for FeO₆ and $\Delta = 6.1 \times 10^{-4}$ for ScO₆. The significant octahedral distortion of FeO₆ is supported by the large QS value obtained by the analysis of Mössbauer spectra. The octahedral distortion of ScO₆ is relatively small compared to that of FeO₆, although Sc³⁺ has a d⁰ electronic configuration.

Intriguingly, the degree of the octahedral distortion for FeO₆ is comparable to that for the second-order Jahn–Teller distortion for d⁰ transition metal ions such as Ti⁴⁺ and Nb⁵⁺; for example, $\Delta = 40 \times 10^{-4}$ for NbO₆ in LiNbO₃,⁵⁸ $\Delta = 33 \times 10^{-4}$ for TiO₆ in LiNbO₃-type FeTiO₃,¹⁷ and $\Delta = 47 \times 10^{-4}$ for TiO₆ in LiNbO₃-type ZnTiO₃.³⁰ Since the second-order Jahn–Teller effect for non-d⁰ magnetic ions is generally small, it is considered that the observed large distortion for FeO₆ in LiNbO₃-type ScFeO₃ originates mainly from the strong electrostatic repulsion between the trivalent Sc and Fe ions in the face-sharing octahedral pairs. On the basis of the atomic displacements from the positions in the centrosymmetric structure, the spontaneous polarization along the *c*-axis is calculated to be about 100 $\mu\text{C}/\text{cm}^2$ using the nominal ionic charges of the constituent ions, in close agreement with that derived from Born effective charges (107 $\mu\text{C}/\text{cm}^2$) (see Supporting Information, section 3). These values, respectively, are larger than the spontaneous polarizations calculated using ionic charges (62 $\mu\text{C}/\text{cm}^2$) and Born effective charges (76 $\mu\text{C}/\text{cm}^2$) for LiNbO₃.^{30,58}

It is also worthwhile to comment on the difference between the isostructural R3*c* phases of ScFeO₃ and BiFeO₃. In the LiNbO₃-type R3*c* phase, the tilting angle about the hexagonal *c*-axis is known to satisfy $\varphi > 20^\circ$; for example, $\varphi = 23.1^\circ$ for LiNbO₃.¹ The octahedral tilting for LiNbO₃-type ScFeO₃ yields $\varphi = 30^\circ$. On the contrary, $\varphi = 13.8^\circ$ for the R3*c* phase of BiFeO₃,⁵⁹ as expected from $t \sim 0.91$, and thus, BiFeO₃ is classified as the perovskite-type oxide with a small magnitude of octahedral tilting, rather than the LiNbO₃-type oxide. It is well-known that in BiFeO₃ the stereochemical effect of 6s² lone pair electrons of Bi³⁺ ions is responsible for the large spontaneous polarization. Instead of such lone-pair active cations, the occupancy of the A-site by small cations induces the polar distortion in ScFeO₃, providing a potentially large spontaneous polarization.

4.3. Magnetic Properties. Since LiNbO₃-type ScFeO₃ and orthorhombic perovskite-type RFeO₃ (R = La–Lu and Y) commonly possess the corner-shared FeO₆ octahedral network, it is interesting to compare the strength of magnetic interactions in the Fe³⁺ sublattice. As already seen in Figure 9, the Fe–O–Fe bond angle for orthorhombic perovskites RFeO₃ decreases from $\alpha = 157^\circ$ for R = La to $\alpha = 141^\circ$ for R = Lu.^{55,56} This should cause the reduction in the Fe–O–Fe superexchange interaction. The T_N in orthorhombic perovskites RFeO₃ decreases from 740 K for R = La to 623 K for R = Lu, following a linear relation between T_N and $\cos^2 \alpha$ ($0.62 < \cos^2 \alpha < 0.84$).⁶⁰ From the extrapolation of this relation, LiNbO₃-type ScFeO₃ [$\alpha = 135.1(3)^\circ$, $\cos^2 \alpha \approx 0.50$] is predicted to have $T_N \sim 560$ K, which is indeed in good agreement with the

experimentally obtained value of 545 K (Figure 10). The slight difference between the predicted and observed T_N may be due

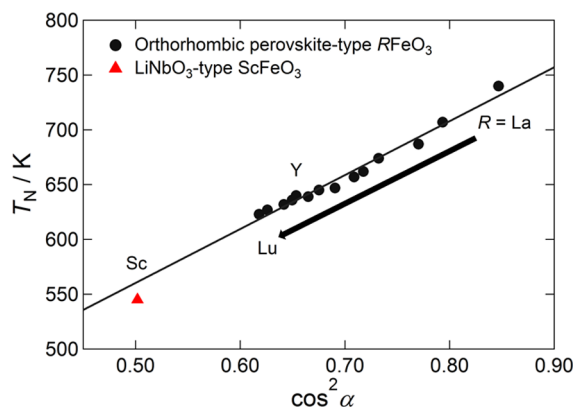


Figure 10. Dependence of Néel temperature (T_N) on the square of cosine of the Fe–O–Fe bond angle ($\cos^2\alpha$) for the LiNbO₃-type ScFeO₃ (this work) and orthorhombic perovskite-type RFeO₃ (R = La–Lu and Y). The black line represents the theoretical curve fitted to the data of orthorhombic perovskites using the equation described in ref 60, showing a linear relation between T_N versus $\cos^2\alpha$. The relation also holds for the LiNbO₃-type ScFeO₃.

to the highly distorted FeO₆ octahedra. The octahedral tilting is a determining parameter for control of physical properties in various perovskite oxides.^{61–63} The present result shows that such a strategy of physical property control in perovskite oxides by the octahedral tilting can be extended to the LiNbO₃-type oxides.

5. SUMMARY

In conclusion, we have successfully obtained a new member of polar magnetic oxides, LiNbO₃-type ScFeO₃, via the high-pressure and high-temperature treatment at 15 GPa and 1450 °C. HAADF-STEM imaging, supported with image simulations, directly demonstrates the highly ordered arrangement of Sc and Fe ions. Using in situ XRD observation, we also found the presence of another new polymorph of ScFeO₃, orthorhombic perovskite-type ScFeO₃, at about 15 GPa and above 800 °C. The orthorhombic perovskite cannot be recovered to ambient pressure but transformed into the LiNbO₃-type structure upon decompression. LiNbO₃-type ScFeO₃ is a promising polar material with a potentially large spontaneous polarization ($\sim 100 \mu\text{C}/\text{cm}^2$). Remarkably, it also exhibits weak ferromagnetism below $T_N = 545$ K due to the canting of antiferromagnetically ordered Fe³⁺ moments within the *ab*-plane; the weakly ferromagnetic component is perpendicular to the *c*-axis, corresponding to the direction of electric polarization. Our results demonstrate that the structure–property relationship (T_N versus octahedral tilting) in perovskite-type oxides is extended to LiNbO₃-type oxides and suggest the possibility of creating new multifunctional materials where several properties can be used simultaneously.

■ ASSOCIATED CONTENT

Supporting Information

Crystallographic data (CIF format), additional data for the sample characterization, and details of the calculations of spontaneous polarization. This material is available free of charge via the Internet at <http://pubs.acs.org>.

■ AUTHOR INFORMATION

Corresponding Author

fujita@dipole7.kuic.kyoto-u.ac.jp

Notes

The authors declare no competing financial interest.

■ ACKNOWLEDGMENTS

This paper presents a result of a joint research program carried out at Geodynamics Research Center, Ehime University. The SXRD and in situ XRD experiments were performed at on the BL02B2 beamline (Proposal Nos. 2010B1715 and 2013A1623) and the BL04B1 beamline (Proposal Nos. 2012B1334 and 2013B1662), respectively, at SPring-8 with the approval of JASRI. The NPD experiment was carried out on the diffractometer WOMBAT at ANSTO's OPAL facility (Proposal No. P3177). Travel costs of T.K. and K.F. were supported by Institute for Solid State Physics, The University of Tokyo (Proposal No. a-03274), JAEA. We thank M. Fukuzumi for the ICP elemental analysis; J. Kim for the SXRD experiment at the BL02B2 beamline; M. Matsushita and H. Etani for the in situ SXRD observation at the BL04B1 beamline; B. Guillaume for the NPD experiment; T. Kuge, S. Hatamoto, and R. Kamakura for the SHG measurement and SEM observation; and I. Tanaka for the first-principles calculations. This research was partly supported by JSPS KAKENHI Grant-in-Aid for Scientific Research (A) (Grant Nos. 25249090 and 25248016) and Scientific Research on Innovative Areas "Nano Informatics" (Grant No. 26106514). S.D.F. acknowledges support under the Discovery Projects funding scheme of the Australian Research Council (Project No. DP110101570).

■ REFERENCES

- (1) Mitchell, R. H. *Perovskites: Modern and Ancient*; Almaz Press: Ontario, Canada, 2002.
- (2) Belik, A. A.; Yi, W. *J. Phys.: Condens. Matter* **2014**, *26*, 163201.
- (3) Hill, N. A. *J. Phys. Chem. B* **2000**, *104*, 6694.
- (4) Wang, J.; Neaton, J. B.; Zheng, H.; Nagarajan, V.; Ogale, S. B.; Liu, B.; Viehland, D.; Vaithyanathan, V.; Schlom, D. G.; Waghmare, U. V.; Spaldin, N. A.; Rabe, K. M.; Wuttig, M.; Ramesh, R. *Science* **2003**, *299*, 1719.
- (5) Kimura, T.; Kawamoto, S.; Yamada, I.; Azuma, M.; Takano, M.; Tokura, Y. *Phys. Rev. B* **2003**, *67*, 180401.
- (6) Azuma, M.; Takata, K.; Saito, T.; Ishiwata, S.; Shimakawa, Y.; Takano, M. *J. Am. Chem. Soc.* **2005**, *127*, 8889.
- (7) Belik, A. A.; Iikubo, S.; Kodama, K.; Igawa, N.; Shamoto, S.-i.; Niitaka, S.; Azuma, M.; Shimakawa, Y.; Takano, M.; Izumi, F.; Takayama-Muromachi, E. *Chem. Mater.* **2006**, *18*, 798.
- (8) Shpanchenko, R. V.; Chernaya, V. V.; Tsirlin, A. A.; Chizhov, P. S.; Sklovsky, D. E.; Antipov, E. V.; Khlybov, E. P.; Pomjakushin, V.; Balagurov, A. M.; Medvedeva, J. E.; Kaul, E. E.; Geibel, C. *Chem. Mater.* **2004**, *16*, 3267.
- (9) Belik, A. A.; Azuma, M.; Saito, T.; Shimakawa, Y.; Takano, M. *Chem. Mater.* **2005**, *17*, 269.
- (10) Syono, Y.; Akimoto, S.; Ishikawa, Y.; Endoh, Y. *J. Phys. Chem. Solids* **1969**, *30*, 1665.
- (11) Syono, Y.; Sawamoto, H.; Akimoto, S. *Solid State Commun.* **1969**, *7*, 713.
- (12) Ito, E.; Matsui, Y. *Phys. Chem. Miner.* **1979**, *4*, 265.
- (13) Ko, J.; Prewitt, C. *Phys. Chem. Miner.* **1988**, *15*, 355.
- (14) Ross, N. L.; Ko, J.; Prewitt, C. T. *Phys. Chem. Miner.* **1989**, *16*, 621.
- (15) Leinenweber, K.; Utsumi, W.; Tsuchida, Y.; Yagi, T.; Kurita, K. *Phys. Chem. Miner.* **1991**, *18*, 244.
- (16) Mehta, A.; Leinenweber, K.; Navrotsky, A.; Akaogi, M. *Phys. Chem. Miner.* **1994**, *21*, 207.

- (17) Leinenweber, K.; Linton, J.; Navrotsky, A.; Fei, Y.; Parise, J. B. *Phys. Chem. Miner.* **1995**, *22*, 251.
- (18) Linton, J. A.; Fei, Y.; Navrotsky, A. *Am. Mineral.* **1997**, *82*, 639.
- (19) Navrotsky, A. *Chem. Mater.* **1998**, *10*, 2787.
- (20) Fennie, C. J. *Phys. Rev. Lett.* **2008**, *100*, 167203.
- (21) Inaguma, Y.; Yoshida, M.; Katsumata, T. *J. Am. Chem. Soc.* **2008**, *130*, 6704.
- (22) Varga, T.; Kumar, A.; Vlahos, E.; Denev, S.; Park, M.; Hong, S.; Sanehira, T.; Wang, Y.; Fennie, C. J.; Streiffer, S. K.; Ke, X.; Schiffer, P.; Gopalan, V.; Mitchell, J. F. *Phys. Rev. Lett.* **2009**, *103*, 047601.
- (23) Belik, A. A.; Furubayashi, T.; Matsushita, Y.; Tanaka, M.; Hishita, S.; Takayama-Muromachi, E. *Angew. Chem.* **2009**, *48*, 6117.
- (24) Inaguma, Y.; Tanka, K.; Tsuchiya, T.; Mori, D.; Katsumata, T.; Ohba, T.; Hiraki, K.; Takahashi, T.; Saitoh, H. *J. Am. Chem. Soc.* **2011**, *133*, 16920.
- (25) Aimi, A.; Katsumata, T.; Mori, D.; Fu, D. S.; Itoh, M.; Kyomen, T.; Hiraki, K.; Takahashi, T.; Inaguma, Y. *Inorg. Chem.* **2011**, *50*, 6392.
- (26) Belik, A. A.; Furubayashi, T.; Yusa, H.; Takayama-Muromachi, E. *J. Am. Chem. Soc.* **2011**, *133*, 9405.
- (27) Arielly, R.; Xu, W. M.; Greenberg, E.; Rozenberg, G. Kh.; Pasternak, M. P.; Garbarino, G.; Clark, S.; Jeanloz, R. *Phys. Rev. B* **2011**, *84*, 094109.
- (28) Li, M.-R.; Walker, D.; Retuerto, M.; Sarkar, T.; Hadermann, J.; Stephens, P. W.; Croft, M.; Ignatov, A.; Grams, C. P.; Hemberger, J.; Nowik, I.; Halasyamani, P. S.; Tran, T. T.; Mukherjee, S.; Dasgupta, T. S.; Greenblatt, M. *Angew. Chem.* **2013**, *52*, 8406.
- (29) Shi, Y.; Guo, Y.; Wang, X.; Princep, A. J.; Khalyavin, D.; Manuel, P.; Michiue, Y.; Sato, A.; Tsuda, K.; Yu, S.; Arai, M.; Shirako, Y.; Akaogi, M.; Wang, N.; Yamaura, K.; Boothroyd, A. T. *Nat. Mater.* **2013**, *12*, 1024.
- (30) Inaguma, Y.; Aimi, A.; Shirako, Y.; Sakurai, D.; Mori, D.; Kojitani, H.; Akaogi, M.; Nakayama, M. *J. Am. Chem. Soc.* **2014**, *136*, 2748.
- (31) Li, M.-R.; Stephens, P. W.; Retuerto, M.; Sarkar, T.; Grams, C. P.; Hemberger, J.; Croft, M. C.; Walker, D.; Greenblatt, M. *J. Am. Chem. Soc.* **2014**, *136*, 8508.
- (32) Glazer, A. M. *Acta Crystallogr., Sect. B* **1972**, *28*, 3384.
- (33) Woodward, P. M. *Acta Crystallogr., Sect. B* **1997**, *53*, 32.
- (34) Megaw, H. D. *Acta Crystallogr., Sect. A* **1968**, *24*, 583.
- (35) Benedek, N. A.; Fennie, C. J. *J. Phys. Chem. C* **2013**, *117*, 13339.
- (36) Li, M.-R.; Adem, U.; McMitchell, S. R. C.; Xu, Z.; Thomas, C. I.; Warren, J. E.; Giap, D. V.; Niu, H.; Wan, X.; Palgrave, R. G.; Schiffmann, F.; Cora, F.; Slater, B.; Burnett, T. L.; Cain, M. G.; Abakumov, A. M.; Van Tendeloo, G.; Thomas, M. F.; Rosseinsky, M. J.; Claridge, J. B. *J. Am. Chem. Soc.* **2012**, *134*, 3737.
- (37) Izumi, F.; Momma, K. *Solid State Phenom.* **2007**, *130*, 15.
- (38) Petricek, V.; Dusek, M.; Palatinus, L. *Z. Kristallogr.* **2014**, *229*, 345.
- (39) Loane, R. F.; Xu, P. R.; Silcox, J. *Acta Crystallogr., Sect. A* **1991**, *47*, 267.
- (40) Momma, K.; Izumi, F. *J. Appl. Crystallogr.* **2011**, *44*, 1272.
- (41) Utsumi, W.; Funakoshi, K.; Katayama, Y.; Yamakata, M.; Okada, T.; Shimomura, O. *J. Phys.: Condens. Matter* **2002**, *14*, 10497.
- (42) Jamieson, J. C.; Fritz, J. N.; Manghnani, M. H. *High-Pressure Res. Geophys.* **1982**, *27*.
- (43) Breard, Y.; Fjellvag, H.; Hauback, B. *Solid State Commun.* **2011**, *151*, 223.
- (44) (a) Brown, I. D.; Altermatt, D. *Acta Crystallogr., Sect. B* **1985**, *41*, 244. (b) The BVS were calculated using the following parameters: $b_0 = 0.37$ for all atoms, $r_0 = 1.849$ for Sc, and $r_0 = 1.759$ for Fe.
- (45) Castillo-Martinez, E.; Bieringer, M.; Shafi, S. P.; Cranswick, L. M. D.; Alario-Franco, M. A. *J. Am. Chem. Soc.* **2011**, *133*, 8552.
- (46) Park, J. H.; Parise, J. B. *Mater. Res. Bull.* **1997**, *32*, 1617.
- (47) Belik, A. A.; Matsushita, Y.; Tanaka, M.; Takayama-Muromachi, E. *Chem. Mater.* **2012**, *24*, 2197.
- (48) Chen, H.; Yu, T.; Gao, P.; Bai, J.; Tao, J.; Tyson, T. A.; Wang, L.; Lalancette, R. *Inorg. Chem.* **2013**, *52*, 9692.
- (49) Belik, A. A.; Matsushita, Y.; Tanaka, M.; Takayama-Muromachi, E. *Inorg. Chem.* **2013**, *52*, 12005.
- (50) Dzyaloshinsky, I. *J. Phys. Chem. Solids* **1958**, *4*, 241.
- (51) Moriya, T. *Phys. Rev.* **1960**, *120*, 91.
- (52) Keune, W.; Date, S. K.; D ezsi, I.; Gonser, U. *J. Appl. Phys.* **1975**, *46*, 3914.
- (53) Eibsch utz, M.; Shtrikman, S.; Treves, D. *Phys. Rev.* **1967**, *156*, 562.
- (54) Ar valo-L pez, A. M.; Attfield, J. P. *Phys. Rev. B* **2013**, *88*, 104416.
- (55) Geller, S.; Wood, E. A. *Acta Crystallogr.* **1956**, *9*, 563.
- (56) Marezio, M.; Remeika, J. P.; Dernier, P. D. *Acta Crystallogr., Sect. B* **1970**, *26*, 2008.
- (57) Shannon, R. D. *Acta Crystallogr., Sect. A* **1976**, *32*, 751.
- (58) Hsu, R.; Maslen, E. N.; Boulay, D. D.; Ishizawa, N. *Acta Crystallogr., Sect. B* **1997**, *53*, 420.
- (59) Kubel, F.; Schmid, H. *Acta Crystallogr., Sect. B* **1990**, *46*, 698.
- (60) Boekema, C.; Van der Woude, F.; Sawatzky, G. A. *Int. J. Magn.* **1972**, *3*, 341.
- (61) Torrance, J. B.; Lacorre, P.; Nazzari, A. I.; Ansaldo, E. J.; Niedermayer, C. *Phys. Rev. B* **1992**, *45*, 8209.
- (62) Kimura, T.; Ishihara, S.; Shintani, H.; Arima, T.; Takahashi, K. T.; Ishizaka, K.; Tokura, Y. *Phys. Rev. B* **2003**, *68*, 060403.
- (63) Goodenough, J. B.; Zhou, J.-S. *J. Mater. Chem.* **2007**, *17*, 2394.